

High-Performance Soft Wearable Robots for Human Augmentation and Gait Rehabilitation

Antonio Di Lallo¹, Shuangyue Yu¹, Tzu-Hao Huang¹, Thomas Bulea²,
Diane Damiano², Hao Su^{1*}

5

¹ *Lab of Biomechatronics and Intelligent Robotics (BIRO), Department of Mechanical Engineering, The City University of New York, City College, NY, 10023, US*

² *Functional and Applied Biomechanics Section, Rehabilitation Medicine Department, Clinical Center, National Institutes of Health, Bethesda, MD, 20892, US*

10

Abstract

Wearable robots are designed to assist people, thus their operation is based on a highly dynamic human-robot interaction. In order to make this interaction as effective as possible, the design of an exoskeleton is subject to challenging requirements 15 involving its mechanical components prior to the control algorithms. Actuator, transmission and wearable structure play a crucial role in determining the performance of a wearable robot. Current high-performance exoskeletons leverage on a new actuation paradigm, so-called quasi-direct drive actuation, to enhance a safe and compliant behavior without renouncing to a high torque density.

20 This chapter goes through the principles behind this new enabling technology and provides demonstrations of its beneficial application on several wearable robots. Three diverse exoskeletal prototypes are showcased, which are designed to assist hip, knee, and back, respectively. Preliminary tests executed on healthy subjects confirm the impactful potential of the quasi-direct drive actuation scheme: all the devices take 25 advantage of low mechanical impedance, high backdrivability, and high torque to exhibit accurate force tracking during various activities.

Keywords: wearable robots, exoskeletons, actuators, quasi-direct drive actuation, soft robots, continuum robots, cable transmission, rehabilitation, physical therapy.

1. Introduction

30 Recent years have seen the development of an increasing number of powered exoskeletal devices for a widening range of applications. Several designs have been proposed either to enhance strength and endurance capabilities in able-bodied subjects [1] or to assist impaired movements in disabled people [2, 3, 4].

35 From a design perspective, wearable robots can be generally classified as rigid or soft in terms of actuation and transmission. If rigid exoskeletons allow to provide the strongest assistance, on the other side, it is recognized that excessive mass and high impedance represent two key drawbacks of such robots [5]. In the tentative of addressing this issue, several designs of soft exoskeletons using pneumatics have been proposed [6]. However, pneumatic actuation typically relies on tethered air 40 compressors, making its application for portable systems still challenging. Therefore, lately, soft cable-driven textile exosuits have become the new trend in wearable robot research [7]. Some examples include exosuits for ankle [8] and hip [2] joint assistance during walking. Thanks to their conformal and compliant structure, these devices are unobtrusive and extremely lightweight, but the absence of rigid links makes their 45 design significantly challenging. The main issues are related to the difficulty of a fixed positioning, especially in correspondence of certain joints (e.g., knee), and to the unavoidable presence of shear forces that usually result annoying for the wearer.

50 Therefore, trying to fill the gap between rigid exoskeletons and soft exosuits, hybrid solutions enable excellent compromises in terms of lightweight, compliance, applied forces and the allowable range of motion. Remarkable performance is made possible thanks to the employment of a new actuation paradigm, purposely designed for highly dynamic interactive tasks. It constitutes a step forward towards the development of “physically intelligent” robots and will disclose a bunch of opportunities for effective human-robot interaction.

55 The rest of the chapter will discuss how the new actuation paradigm allows dynamic interactive tasks when it is employed to power wearable robots. In Sec. 2, the involved actuation technologies are described, while Sec. 3 presents its application to three kinds of exoskeletons for hip, knee, and back assistance. Finally, conclusions are discussed in Sec. 4.

60 **2. Actuation Technologies for Physical Human-Robot Interaction**

Safe and dynamic interaction with humans is of paramount importance for collaborative robots. Recent exoskeletons focus on advanced algorithms to improve control performance [2, 9, 10, 11, 12, 13], while there is limited work in actuation hardware design.

65 Yet, observations from nature have highlighted that body properties of biological organisms have a key function in providing “physical intelligence” during dynamic interactive tasks. In the same manner, the mechanical design of robots’ hardware represents an opportunity to provide embedded intelligence, which is a sort of intelligence intrinsic to the system without relying on complicated control algorithms
70 [14].

When dealing with wearable robots, indeed actuators play the greatest role among the various mechanical components.

75 Besides actuator prototypes for soft material robots, state-of-the-art wearable robots include three primary actuation methods, namely, conventional geared actuation, series elastic actuation (SEA), and quasi-direct drive actuation (QDD, also known as proprioceptive actuation) [14, 15, 16]. Some significant examples are reported in Fig. 1.

Exoskeletons	[17]	[18,19]	[20]	[15]
Actuation Paradigm	Conventional actuation	Series Elastic Actuation	Conventional actuation & textile wearable	Quasi-Direct Drive actuation
	High gear ratio Conventional motor	High ratio gearbox Conventional motor load & Wearable Spring, encoder	High gear ratio Conventional motor load & Wearable	High torque density motor Low ratio gearbox load & Wearable
Torque (Nm)	70	60	32	48
Mass (kg)	23	7	5	3
Bandwidth (Hz)	5	5	20	44
Backdrive torque (Nm)	30	9	N/A	0.4
Torque Density (Nm/kg)	3	8.6	6.4	16

80 Fig. 1 Exemplifying embodiments of the main actuation methods employed in wearable robots [14]. They include conventional geared actuators, in both rigid [17] and textile exosuits, series elastic actuators [18, 19], and [20] quasi-direct drive actuators [15]. Green, yellow and red shaded areas indicate relatively high, middle, and low performance, respectively.

85 Conventional actuation uses high-speed and low-torque motors (typically brushless direct current motors, BLDC) coupled to high gear ratio transmission [3, 17, 21, 22]. It can meet typical requirements related to assistive torque, angular velocity, and control bandwidth, but suffers from high mechanical impedance, which makes the overall system quite resistant to free movements of the wearer. Although control 90 algorithms might be able to partially compensate for the undesirable impedance, a complete suppression of the obtrusive effects due to the high inertia of the actuator remains unfeasible.

95 Series elastic actuators (including parallel elastic actuators and other variable stiffness elastic actuators) overcome the low-compliance limitation [19, 23, 18, 24] using spring-type elastic elements. However, this solution is detrimental to the system simplicity, lightweight and bulkiness, and leads to sacrifice the performance in control bandwidth, resulting in limited practical benefits for wearable robots.

Quasi direct-drive actuation instead involves a change of perspective. Being composed of high-torque motors and low gear ratio transmission, it exhibits intrinsic high torque density, high bandwidth, and high backdrivability, meeting all the

multifaceted requirements of versatile wearable robots. Therefore, these features
100 identify QDD actuation as a promising technology for dynamic human-robot interaction, whose feasibility has already been proved in several preliminary tethered exoskeletons [7, 25, 26, 27]. Other recent results are reported in Sec. 3 about wearable robots for hip, knee, and back assistance.

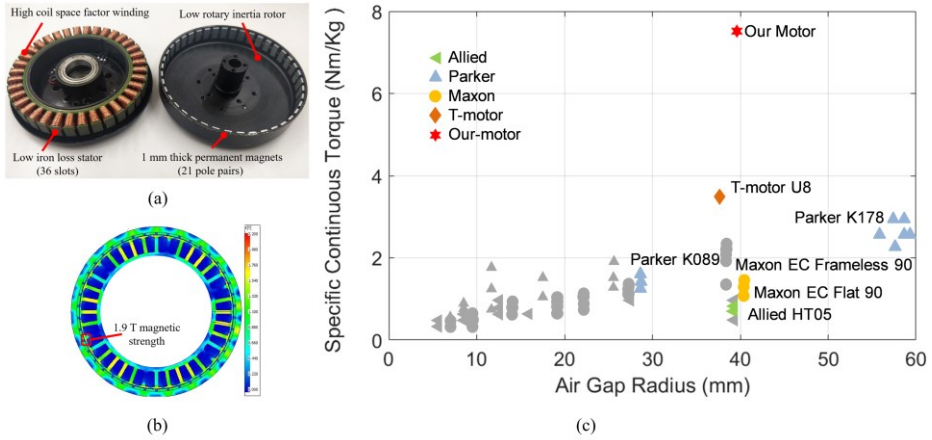
2.1 High Torque Density Motors

105 Quasi-direct drive actuation is a new paradigm of robot actuation design that leverages high torque density motors with low ratio transmission mechanisms [14, 28]. It has been recently studied for legged robots [14] and exoskeletons [29].

110 Benefits of high torque density actuation include a simplified mechanical structure with reduced mass and volume, and high compliance, i.e., high backdrivability. Thus, it is an ideal candidate to satisfy the static and dynamic requirements of wearable robots.

115 A crucial component for the design of high torque density actuation is the high torque density motor. In [30] a custom BLDC motor is designed with optimized mechanical structure, topology, and electromagnetic properties. It uses high-temperature resistive magnetic materials and adopts an outer rotor and a flat, concentrated winding structure to maximize the torque density [31, 32]. As shown in Fig. 2(a), in order to enhance the efficiency the motor uses fractional-slot type winding, which allows to reduce the cogging torque and to minimize the copper loss. It has 21 pole pairs and 36 rotor slots, a number significantly higher than the 12 pole
120 pairs of the commercial motor Maxon EC90 [23] or the 10 pole pairs and 18 rotor slots of another concurrent research prototype [33]. Moreover, unlike conventional BLDC motors that place windings around the rotor, here motor winding is attached to the stators, and the rotor consists only of the cover and 1 mm thick permanent magnet chips. In this way, the lightweight exterior rotor reduces rotary inertia and increases
125 the torque to inertia ratio. Finally, a further detail not to be neglected involves the choice of the electromagnetic material: permanent magnets are made of sintered

Neodymium Iron Boron (NdFeB), which can reach 1.9 T magnetic field intensity, as resulting from finite element analysis reported in Fig. 2(b).

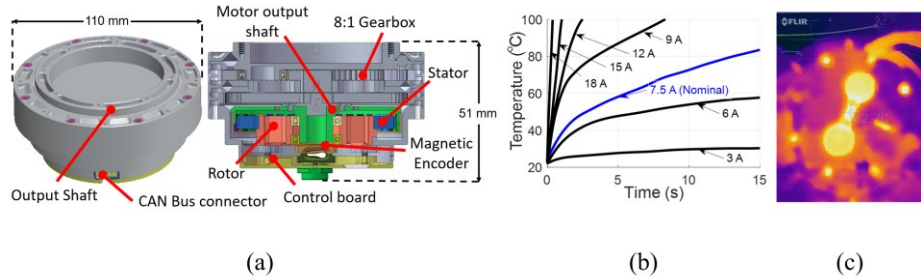


130 Fig. 2 (a) Design of custom brushless DC electric motor (BLDC) with the exterior
 135 rotor and concentrated winding. The fractional slot design (36 slots, 21 pole pairs)
 140 allows to reduce cogging torque and to minimize copper loss [33]. (b) Finite element
 analysis shows that by using sintered Neodymium Iron Boron permanent magnets the
 magnetic strength of the stator can reach 1.9 T, under the condition of no current in
 the winding. (c) Distribution of continuous torque density versus air gap radius for our
 custom motor compared to commercial ones. It is worth noting that exoskeletons
 typically need motors with an air gap radius in the 35-40 mm range. Our custom
 motor, marked with a star in the plot, has continuous torque density (7.81 Nm/Kg)
 10.4 times higher than the Maxon brushless DC motor EC flat 90 (#323772,
 0.75 Nm/Kg), widely used in exoskeleton industry.

Overall, this design allows to significantly reduce the inertia and mechanical impedance of the motor while increasing its control bandwidth. It weighs 256 g and provides 2 Nm continuous torque. Fig. 2(c) shows the distribution of continuous torque density versus air gap radius for this motor compared to commercial ones [28]. In the 35-40 mm air gap radius domain, usually adopted for wearable robots, the continuous torque density of the described motor is 7.81 Nm/kg, remarkably higher than the values of the widely used T-motor U8 (3.5 Nm/kg) and Maxon EC Flat 90 (#323772, 0.75 Nm/kg).

2.2 Quasi-Direct Drive Actuation

150 The high torque density motor constitutes an important step towards an effective actuation strategy for wearable robots. To keep the system compact and lightweight, it is worth combining the motor with all the related components in a fully integrated actuator, as shown in Fig. 3(a) [34, 35].



155 Fig. 3 (a) Fully integrated quasi-direct drive actuator, including the high torque density motor, an 8:1 gearbox, a magnetic encoder, and control electronics. It is compact ($\Phi 110$ mm \times 52 mm height), lightweight (777 g) and able to generate high torque (16 Nm nominal torque and 45 Nm peak torque). (b) Stator temperature over time under different current conditions. (c) Thermal image after 15 min of continuous 160 7.5 A current operation shows that the actuator surface reaches a temperature of 62.7°C.

The overall actuator weight is 777 g and it includes the high torque density motor, an 8:1 ratio planetary gear, a 14 bits high accuracy magnetic encoder, and a wide range input (10-60 V) motor driver and controller.

165 Detailed specifications of the resulting actuator can be found in Table I, together with the corresponding values of a reference example from conventional actuators and series elastic actuators.

TABLE I PERFORMANCE COMPARISON OF THE THREE MAIN ACTUATION PARADIGMS

Parameter	Unit	Conventional [21]	SEA [23]	Presented QDD
Output rated torque	Nm	8	40	17.5
Actuator mass	kg	~0.50	1.80	0.77
Actuator rated torque density	Nm/kg	16	22.2	20.7
Control bandwidth	Hz	5.1	4.2	73.3

Back-drive torque	Nm	-	-	0.97
-------------------	----	---	---	------

170 Low-level control on position, velocity, and current is implemented in the driver-control electronics, whereas real-time information for high-level control transfer through the Controller Area Network (CAN bus) communication protocol.

175 When powered with a nominal voltage of 42 V, the actuator reaches a nominal speed of 188 RPM (19.7 rad/s). Moreover, thanks to the quasi-direct drive strategy using low gear ratio transmission, the actuator presents low output inertia ($57.6 \text{ kg}\cdot\text{cm}^2$), which means low resistance to natural human movements.

180 Regarding the output capability, it is worth noting that it is highly limited by the motor's winding temperature. To evaluate the actuator working current performance, it was operated continuously in stall mode under different output currents. The stator temperature was measured by an embedded temperature sensor and the surface temperature was measured by a portable FLIR® thermal camera. The experiment was performed in a 22°C lab environment without external heat dissipation. The maximum operating time was set to 15 mins and the maximum temperature of the stator to 100°C. In Fig. 3(b) the evolution over time of the stator temperature is plotted for 185 different current conditions, while Fig. 3(c) shows the thermal camera image of the actuator surface after 15 min under 7.5 A nominal current, demonstrating that the highest temperature of 62.7°C is reached. This experiment proves that the actuator can produce a continuous output torque of 17.5 Nm under 7.5 A rated current.

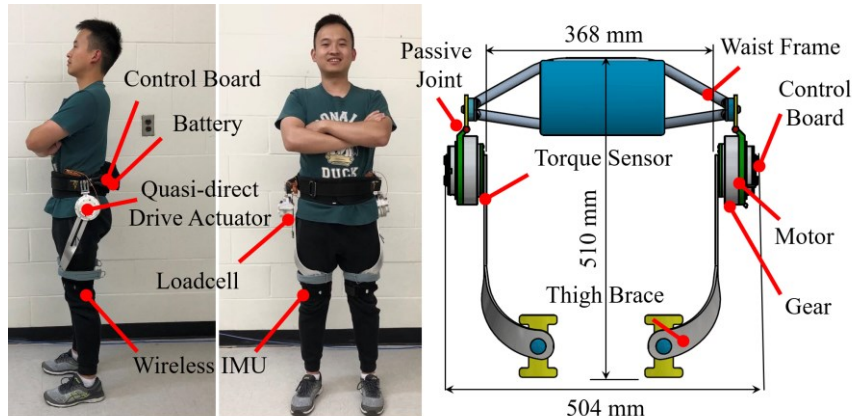
3. Applications to Wearable Robots

190 Having discussed the properties of QDD actuation and its potential impact on applications involving dynamic human-robot interaction, this section will analyze in detail three different use cases: a portable exoskeleton for hip assistance during walking and squatting, and two tethered versions, one for knee support during squatting and the other for back assistance in stoop lifting.

195 3.1 *Hip Exoskeleton*

During walking, human hip joints have flexion/extension movements in the sagittal plane and abduction/adduction movements in the frontal plane. Therefore, a hip exoskeleton needs to accommodate those two degrees of freedom. For level-ground walking, the range of motion of a human hip joint is 32.2° flexion, 22.5° extension, 200 7.9° abduction, and adduction 6.4° [36]. Here the robot is designed with a larger range of motion than the standard requirements to handle a heterogeneous population for a wide variety of activities beyond walking, such as squatting, sitting, and stair climbing. Moreover, it was observed that for a human of 75 kg walking at 1.25 m/s the peak torque and the speed of the hip joint are 97 Nm and 3.5 rad/s, respectively, 205 but results in [37] and [38] show that a 12 Nm torque assistance is sufficient to produce a 15.5% reduction in metabolic cost for uphill walking.

3.1.1 *Design*



210 Fig. 4 The hip exoskeleton is composed of a waist frame, two QDD actuators, two torque sensors, and two thigh braces. It provides assistance for flexion and extension of the hip joints in the sagittal plane, while passive joints allow free abduction and adduction movements.

The mechanical system of the hip exoskeleton is symmetric about the sagittal plane and is mainly composed of a waist frame, two actuators, two torque sensors, and two

thigh braces, as shown in Fig. 4. The waist frame has the main function of anchoring
215 the actuators. It has a curvature conformal to the wearer's pelvis, enabling uniform
force distribution on the human body. A wide waist belt is used to attach the waist
frame to the user, aiming at maximizing the contact area so as to reduce the pressure
on the human. The motor housings are connected to the waist frame by means of
hinge joints that enable passive degrees of freedom in the frontal plane (e.g.,
220 abduction and adduction), whereas the actuators work in the sagittal plane to assist the
flexion and extension of the hip joints. A customized compact torque sensor is
assembled to the output flange of the actuator to measure the output torque. Finally,
the thigh brace is fixed to the sensor and transmits the actuator torque to the wearer's
thigh thanks to a fastening strap. It is worth noting that in order to alleviate the wearer
225 from painful shear forces, the thigh brace has a curved structure that enables to
provide assistive forces on the thigh perpendicularly to the frontal plane.

Regarding the electrical system, it supports high-level torque control, low-level
motor control, sensor signal conditioning, data communication, and power
management. The local motor controller is developed based on a motor driver and a
230 DSP microcontroller. It allows to measure the motor motion status and to realize
control based on current, velocity, and position. The high-level microcontroller runs
on Arduino Due and performs torque control. It acquires real-time data on the lower-
limb posture from the wireless IMU sensors and on the applied torques from the
loadcells.

235 3.1.2 ***Modeling***

The overall system can be decomposed into four main subsystems, as shown in
Fig. 5: the motor, the transmission mechanism, the wearable structure, and the human
leg. Connections between these modules are represented as springs and dampers to
model the force and motion transmission.

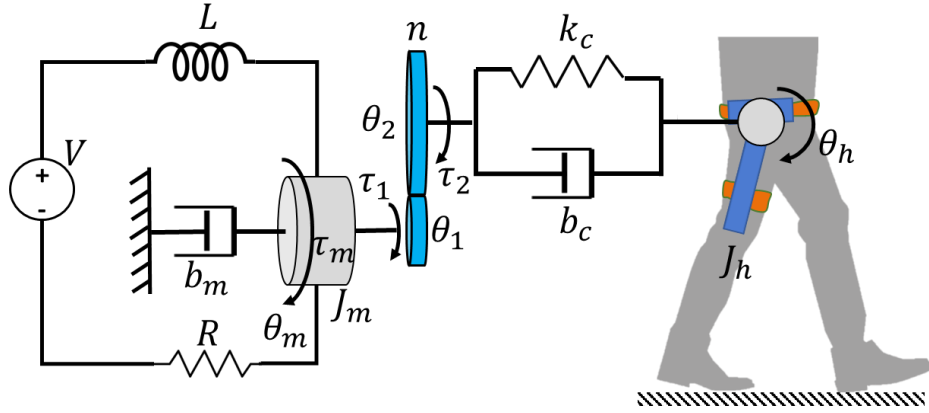


Fig. 5 Human-exoskeleton coupled dynamic model. It consists of four subsystems: motor, transmission, wearable structure, and human leg.

The dynamics of the motor electrical system can be characterized by the winding resistance R and inductance L . Subject to input voltage V , the motor generates a torque τ_m proportional to the current i and to the torque constant k_t , whereas the back-electromagnetic force V_b is proportional to the motor velocity $\dot{\theta}_m$ and to the constant k_b . Therefore, the governing equations of the motor electrical system are

$$V - V_b = L \frac{di}{dt} + Ri \quad (1)$$

$$\tau_m = k_t i \quad (2)$$

$$V_b = k_b \dot{\theta}_m. \quad (3)$$

Meanwhile, from a mechanical perspective, the motor is described by the equation

$$\tau_m = J_m \ddot{\theta}_m + b_m \dot{\theta}_m + \tau_1, \quad (4)$$

where J_m denotes the moment of inertia of the rotor around its rotation axis, b_m is the damping coefficient that takes into account internal viscous friction, θ_m denotes the motor angle, and τ_1 is the torque applied to the output shaft.

Then, considering a gearbox with gear ratio $n:1$, it has the effect of reducing the angular velocity and amplifying the torque according to the equations

$$\theta_1 = \theta_m; \quad \theta_2 = \frac{\theta_1}{n}; \quad \tau_2 = n\tau_1. \quad (5)$$

In eq. (5), θ_1 and θ_2 denote the rotation angles of the input and output shafts of the gearbox, respectively, and τ_1 and τ_2 the corresponding applied torques.

The wearable structure of the exoskeleton can be designed with rigid linkages, springs, cable-pulley systems, cable-textile systems. In all the cases, it can be modeled through global parameters, namely stiffness k_c and damping b_c . Therefore, the resulting equation for the dynamics of the wearable structure is

$$\tau_2 = b_c(\dot{\theta}_2 - \dot{\theta}_h) + k_c(\theta_2 - \theta_h). \quad (6)$$

260 Finally, the human limb is governed by the equation

$$J_t \ddot{\theta}_h + b_c(\dot{\theta}_h - \dot{\theta}_2) + k_c(\theta_h - \theta_2) = \tau_l, \quad (7)$$

where J_t is the inertia of the limb with the orthosis, θ_h is the hip rotation angle, τ_l is the human torque generated by the muscles, and τ_a is the torque applied to the human thigh. τ_a can be an assistive or resistive torque and can be calculated as

$$\tau_a = \tau_2 = b_c\left(\frac{\dot{\theta}_m}{n} - \dot{\theta}_h\right) + k_c\left(\frac{\theta_m}{n} - \theta_h\right). \quad (8)$$

Assume as initial condition $\theta_h(0)$, $\dot{\theta}_h(0)$ and $V(0)$ equal to zero and neglect the 265 inductance L due to its small value [39]. Let s be the Laplace variable, in the s -domain the assistive torque $\tau_a(s)$ is related to the hip rotation angle $\theta_h(s)$ and input voltage $V(s)$ as expressed in eq. (9).

$$\tau_a(s) = G_1(s)V(s) + G_2(s)\theta_h(s) = n_1(s) \left[\frac{n_2(s)}{d(s)}V(s) + \frac{n_3(s)}{d(s)}\theta_h(s) \right], \quad (9)$$

where

$$\begin{aligned} n_1(s) &= (b_c s + k_c) \\ n_2(s) &= n k_t \\ n_3(s) &= -n^2 [J_m R s^2 + (R b_m + k_b k_t) s] \\ d(s) &= J_e s^2 + b_e s + k_e \\ J_e &= n^2 J_m R; \quad b_e = n^2 R b_m + n^2 k_b k_t + R b_c; \quad k_e = R k_c. \end{aligned} \quad (10)$$

The natural frequency ω_n of the open-loop torque control for the second-order 270 system is

$$\omega_n = \sqrt{\frac{k_e}{J_e}} = \sqrt{\frac{R k_c}{n^2 J_m R}} = \sqrt{\frac{k_c}{n^2 J_m}}. \quad (11)$$

The effective moment of inertia J_e is equal to $n^2 J_m$, hence the natural frequency ω_n of the open-loop torque control is directly proportional to wearable structure

stiffness k_c and inversely proportional to the square of the gear ratio n and the moment of inertia of the motor J_m .

275 The described model allows also to make some considerations about the backdrivability. To identify the property of the passive mechanism, $V(s)$ is set to zero and the output resistive torque τ_a induced by the human motion $\theta_h(s)$ can be derived from eq. (12), while eq. (13) provides the output link impedance.

$$\tau_a(s) = G_2(s)\theta_h(s) = \frac{-(b_c s + k_c)n^2[J_m R s^2 + (R b_m + k_b k_t)s]}{n^2[J_m R s^2 + (R b_m + k_b k_t)s] + R b_c s + R k_c} \theta_h(s) \quad (12)$$

$$Z_o(s) = \frac{\tau_a(s)}{s\theta_h(s)} \quad (13)$$

As the gear ratio is sufficiently small, the resistive torque can be neglected, because

$$\lim_{n \rightarrow 0} \tau_a(s) = 0 \quad (14)$$

280 As the gear ratio is large enough, the resistive torque is approximated by eq. (15), where the wearable structure damping b_c and stiffness k_c are the dominating terms.

$$\lim_{n \rightarrow \infty} \tau_a(s) \approx -(b_c s + k_c) \theta_h(s) \quad (15)$$

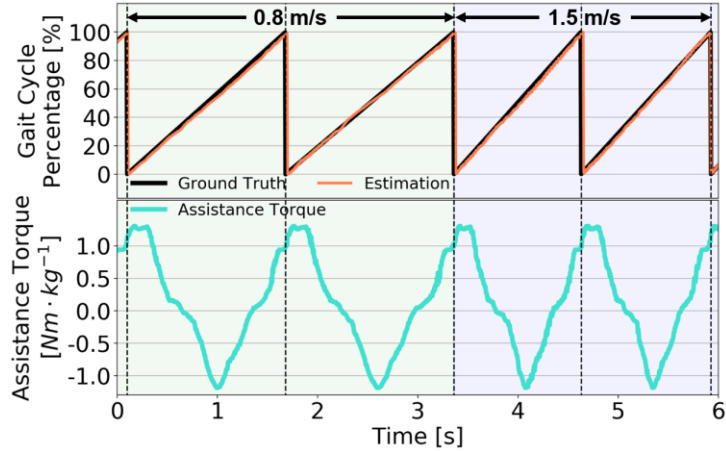
When the gear ratio is equal to 1, the resistive torque is expressed by eq. (16). It depends on the gear ratio n , the damping term b_c , the stiffness k_c , the motor inertia J_m , the motor damping b_m , the motor resistance R , the motor torque constant k_t , 285 and the back EMF constant k_b .

$$\tau_a(s)|_{n=1} = -\frac{(b_c s + k_c)(J_m R s^2 + R b_m s + k_b k_t s)}{J_m R s^2 + (R b_m + k_b k_t + R b_c)s + R k_c} \theta_h(s) \quad (16)$$

Therefore, from Eqs. (14), (15), and (16) it is clear that high backdrivability (i.e. low resistive torque and low output impedance) can be achieved with small gear ratio n , small damping constant b_c , and small stiffness k_c .

3.1.3 *Control*

290 The control system is based on a hierarchical architecture composed of a high-level control layer that robustly detects gait intention (Fig. 6 top), a middle-level control that generates the assistive torque profile (Fig. 6 bottom), and a low-level control layer that implements a current-based torque control.



295 Fig. 6 (Top) Comparison between ground truth (black) and estimated (orange) gait cycle percentage. The first is calculated offline by insole signals, while the estimation is provided by applying a regression method to information from IMUs. The robust gait recognition ($R^2=0.997$) is able to compensate for the disturbances due to walking speed changes. (Bottom) Assistive torque profile generated by the control algorithm.

300 An algorithm based on a data-driven method [40] with a neural network regressor is used to compensate for the uncertainties caused by changing gait speeds. It estimates the walking and squatting cycle percentage in real-time by the signals from two inertial measurement units (IMUs) mounted on the anterior of both thighs (Fig. 4). These sensors provide motion information, including Euler angles, angular 305 velocities, and accelerations at a frequency of 200 Hz. Motion information during the last 0.4 s sliding time window constitutes the input vector of the neural network for both offline training process and online control. The neural network used in this algorithm has one hidden layer with 30 neurons as well as a sigmoid activation function and deploys the Xavier initialization [41] for the network weights. The 310 algorithm could achieve an $R^2 = 0.997$ on a test set of walking and squatting data collected from three able-bodied subjects at several different speeds.

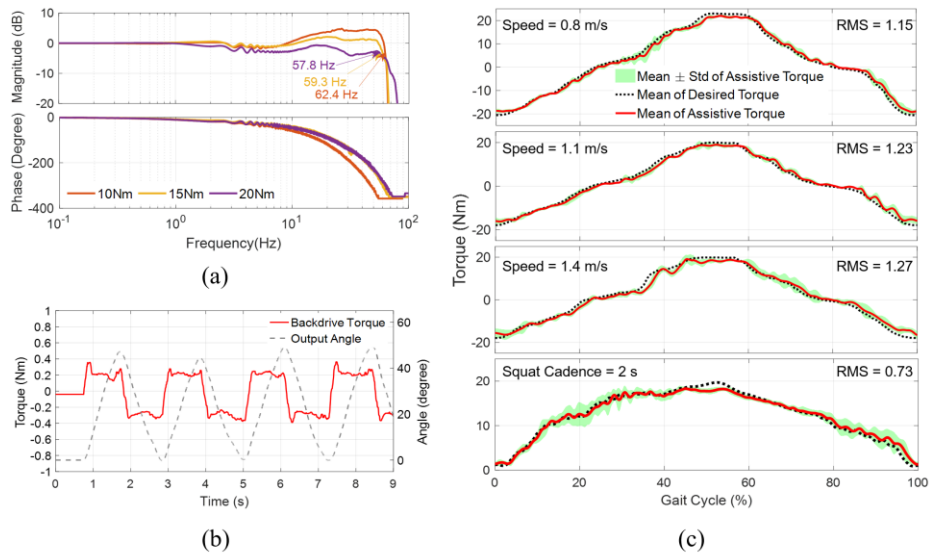
315 After obtaining the gait percentage, the middle-level controller calculates the assistive torque according to a predefined torque profile expressed as a look-up table. Basically, the desired assistive torque is obtained searching the gait percentage in the look-up table and using interpolation to fill-in missing data. The predefined torque

profile for walking is generated by the human biological model in [42], while the one for squatting is expressed as a simple sine wave.

Finally, the low-level torque control architecture is composed of an inner and outer loop control. The inner loop implements motor current control in the local motor controller, while the outer loop performs torque control in Arduino Due using feedback signals from motors, loadcells, and IMU-based gait recognition.

3.1.4 Evaluation

Several experiments were conducted on the hip exoskeleton to characterize its mechanical versatility through backdrivability and bandwidth demonstrations.



325

330

335

Fig. 7 (a) Bode plot of the 10 Nm, 15 Nm, and 20 Nm torque control, demonstrating remarkably high control bandwidth. (b) Back-drive torque measured in unpowered mode for the imposed joint angular displacement. The maximum resistance torque is approximately 0.4 Nm, significantly lower than other state-of-the-art devices (e.g. 2 Nm in [19] and 1 Nm in [33]). (c) Torque tracking performance of assistance (peak torque is limited to ± 20 Nm) during walking and squatting tests. The mean of actual assistive torque (red) is able to track the desired torque (black dash) with high accuracy. RMSEs of torque tracking (0.8 m/s, 1.1 m/s and 1.4 m/s walking, 2 s cadence squatting) are 1.15 Nm, 1.23 Nm, 1.27 Nm and 0.73 Nm respectively (5.75%, 6.15%, 6.35% and 3.65% of the peak torque).

For the bandwidth experiment chirp signals with different magnitudes were used as reference torque to obtain the Bode plot. The results are shown in Fig. 7(a), where bandwidth values of 57.8 Hz, 59.3 Hz, and 62.4 Hz are obtained for 10 Nm, 15 Nm and 20 Nm chirp magnitude respectively. Thus, the bandwidth is much higher than
340 the requirement of human walking, but this property turns out to be useful for agile human activities, e.g. running and balance control to unexpected external disturbance. Compared with the exoskeleton using SEA [19], characterized by 5 Hz bandwidth, a high control bandwidth robot is safer and more robust to uncertainties.

For the backdrivability experiment, instead, the back-drive torque was measured in
345 unpowered mode. An angular displacement of 32.2° was imposed on the hip joint at 1 Hz frequency while the actuator was turned off and the resistance torque was measured. The profiles of the rotation angle and the back-drive torque are reported in Fig. 7(b). Results show that the hip exoskeleton presents a very low back-drive torque (maximum value is about 0.4 Nm), demonstrating higher compliance than other state-
350 of-the-art exoskeletons [19, 33].

As last experiment, a control test was performed to investigate the torque tracking performance of the hip exoskeleton. It was tested during treadmill walking with varying speed from 0.8 m/s to 1.4 m/s and during squatting with 2 s cadence. A total of 15 tests with the same torque profile were performed for each of the walking and
355 squatting motions. The tracking performance of hip assistance is shown in Fig. 7(c). The average RMSE between the desired and actual torque trajectory in 60 tests is 1.09 Nm (5.4% of the maximum desired torque). This result indicates that the torque controller is able to track with high accuracy the desired assistance during walking and squatting.

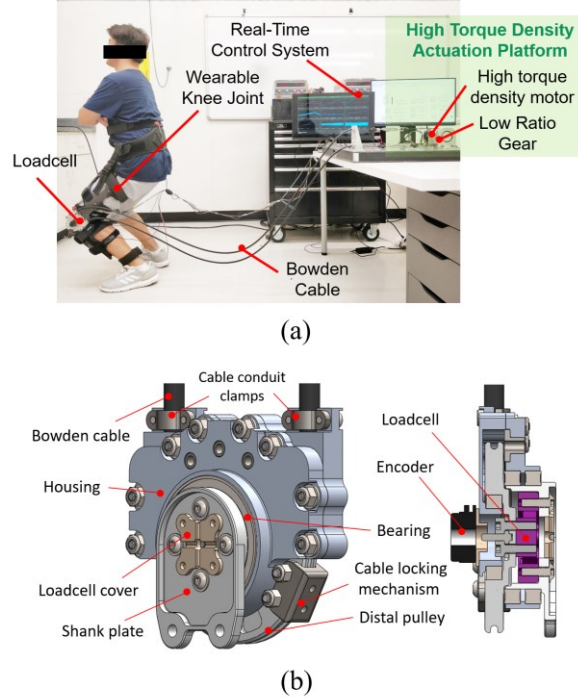
360 3.2 *Knee Exoskeleton*

Recently there is a growing interest in wearable robots for knee joint assistance as cumulative knee disorders account for 65% of lower extremity musculoskeletal disorders. Squatting and kneeling are two of the primary risk factors that contribute to knee disorders [43].

365 Knee joint assistance during squatting necessitates a broad range of motion (0-130° flexion) and joint torque (up to 60 Nm) [44]. Moreover, for an effective synchronization with the wearer, the torque generated from the robot needs to be delivered at an angular velocity of no less than 2.4 rad/s.

3.2.1 ***Design***

370 Most of the existing knee exoskeletons are designed for walking assistance [45, 46] and they typically do not allow squat motion due to the interference between the robot structure and human bodies (e.g. [47, 48]). Since the focus of the work is to understand the feasibility of the approach for squat assistance, the exoskeleton consists of a wearable robot emulator, that is a tethered wearable structure with 375 offboard actuation. Fig. 8(a) shows the overall system, including the wearable structure, a bidirectional Bowden cable transmission mechanism and the high torque density actuator implemented as a tethered platform. It is worth noting that though the current platform is configured as a tethered system, it can be easily converted to a portable system, as the overall mass of motor and gears is 0.55 kg.



380

Fig. 8 (a) The hip exoskeleton includes the wearable structure with the knee joint mechanism, a bidirectional Bowden cable transmission system, and a high torque density actuation platform. (b) Section view (left) and isometric view (right) of the cable-driven knee joint mechanism for bidirectional actuation, i.e. knee flexion and extension.

385

The bidirectional Bowden cable mechanism (similar to [49] and [50]) uses a single motor to generate bidirectional actuation, i.e. knee flexion and extension. In this regard, a key role is played by the knee joint mechanism (Fig. 8(b)), which constitutes the distal portion of the bidirectional cable-drive mechanism. It is designed to be lightweight and low-profile, namely to avoid interference with the human body during squat motion.

390

The assembly includes one flexion cable and one extension cable that pass around the distal pulley and terminate at the cable locking mechanism. One side of the knee mechanism is attached to the thigh brace while the shank plate is fixed to the calf brace. A load cell connects the thigh and the calf links and plays a key role in force transmission between the cable and the shank plates. In fact, when the cable is pulled,

395

it actuates the pulley through the locking mechanism and drives the shank plate via the loadcell.

The exoskeleton is attached to the body via 3D printed carbon fiber braces designed to be conformal to the human leg. Thanks to these braces the torque at the knee joint is converted into pressure distributed along the length of the thigh and the shank. Therefore, the size of the wearable arms plays a crucial role in the performance and user comfort. Three-dimensional infrared scans (Sense 2, MatterHackers Inc.) of the wearer's leg are taken and processed into a CAD model. This model is then 3D printed using fused deposition modeling with carbon fiber reinforcements. Foam paddings are also added in the locations of leg contact to aid in comfort, while velcro straps are used to anchor the exoskeleton arms to the leg.

3.2.2 ***Modeling***

A human biomechanics model is derived to calculate the knee joint torque to assist both squat and stoop lifting activities in real-time. Unlike methods that use simple and predefined profiles (e.g. sine waves) to approximate the human joint torque, this method is biologically meaningful and applicable to squat, stoop and walking activities. In [51] an assistive algorithm for a squat assistance exoskeleton is proposed assuming that the back of the subject is straight, and the trunk angle is zero. It only uses the knee joint angle to calculate the required torque and lacks the posture information of the hip and trunk. However, during lifting (squat and stoop) the back angle varies and significantly affects the knee joint torque.

Since squat and stoop involve significantly different biomechanics of the knee joint, this model is versatile in the sense that it can cover both scenarios for a wide variety of people. The knee joint torque $\hat{\tau}_k$ can be derived from eq. (17)

$$\hat{\tau}_k = I(\theta)\ddot{\theta} + C(\theta, \dot{\theta})\dot{\theta} + G(\theta), \quad (17)$$

420 where θ is the joint angles, $I(\theta)$ is the inertia matrix, $C(\theta, \dot{\theta})$ denotes the centrifugal and Coriolis term, and $G(\theta)$ is the gravitational loading.



Fig. 9 Quasi-static model used to derive the assistive knee joint torque during squat motion.

As typically lifting tasks are relatively slow, the knee joint torque is dominated by
 425 gravitational loading. Thus, with reference to Fig. 9, estimated knee joint torque $\hat{\tau}_k$ can be computed using a quasi-static model, as expressed in eq. (18).

$$\hat{\tau}_k = G(\theta) = -0.5[M_b g(L_b \sin \theta_b + L_t \sin \theta_t) + M_t g L_{tc} \sin \theta_t] \quad (18)$$

Here the knee extension is defined as the positive direction for the knee joint torque $\hat{\tau}_k$, while the clockwise direction is defined as the positive direction for the trunk angle θ_b , the thigh angle θ_t , and the shank angle θ_s . M_b is the combined mass of the head, neck, thorax, abdomen, pelvis, arms, forearms, and hands, M_t is the mass of thigh, L_b is the length between the center of mass M_b and the hip pivot, L_t is the length of thigh between the hip and the knee pivots, L_{tc} is the length between the center of mass M_t and the knee pivot, and g is the gravitational constant. The parameters L_b , L_t , L_{tc} , M_b , M_t are calculated according to Eqs. (19)-
 430 (23) using data in Table II obtained from anthropometry research [52]. It is worth noting that the proposed model is customizable to different individuals because the assistive torque can be adjusted to the subject's weight and height by means of the weight ratio (ratio between the subject weight M_{sb} and the human model weight M_W) and the height ratio (ratio between the subject height L_{sb} and the human model
 435 height L_H .
 440

TABLE II THE HUMAN SEGMENT PARAMETERS

#	Segment	M_i : Mass (Kg) Total Weight M_W : 81.4 Kg	L_i : Length between Center of Mass to Ground (m) Total Height L_H : 1.784 m
1	Head	M_1 : 4.2 Kg	L_1 : 1.679 m
2	Neck	M_2 : 1.1 Kg	L_2 : 1.545 m
3	Thorax	M_3 : 24.9 Kg	L_3 : 1.308 m
4	Abdomen	M_4 : 2.4 Kg	L_4 : 1.099 m
5	Pelvis	M_5 : 11.8 Kg	L_5 : 0.983 m
6	Arms	M_6 : 4 Kg	L_6 : 1.285 m
7	Forearms	M_7 : 2.8 Kg	L_7 : 1.027 m
8	Hands	M_8 : 1 Kg	L_8 : 0.792 m
9	Thighs	M_9 : 19.6 Kg	L_9 : 0.75 m
10	Calfs	M_{10} : 7.6 Kg	L_{10} : 0.33 m
11	Feet	M_{11} : 2 Kg	L_{11} : 0.028 m
12	Hip Pivot to Ground		L_{12} : 0.946 m
13	Knee Pivot to Ground		L_{13} : 0.505 m

$$M_b = (M_{sb}/M_W) \cdot \sum_{i=1}^8 M_i \quad (19)$$

$$M_t = (M_{sb}/M_W) \cdot M_9 \quad (20)$$

$$L_b = (L_{sb}/L_H) \cdot \{ [\sum_{i=1}^8 (M_i \cdot L_i) / \sum_{i=1}^8 (M_i)] - L_{12} \} \quad (21)$$

$$L_t = (L_{sb}/L_H) \cdot (L_{12} - L_{13}) \quad (22)$$

$$L_{tc} = (L_{sb}/L_H) \cdot (L_9 - L_{13}) \quad (23)$$

Finally, given the estimated joint torque $\hat{\tau}_k$, the desired assistive torque τ_r to be provided by the exoskeleton is defined as

$$\tau_r = \alpha \cdot \hat{\tau}_k. \quad (24)$$

As long as the gain α is positive, the exoskeleton will assist the human. It can be used to reduce the loading and increase the endurance of workers. On the other hand, when the gain α is negative, the exoskeleton will resist the human. It can be useful to increase the muscle strength for healthy subjects in fitness or individuals with movement impairments in rehabilitation.

3.2.3 Control

The control system is based on a two-level configuration architecture, as shown in Fig. 10: a target computer is used for high-level assistive control, while local motor driver electronics perform low-level control. The control strategy follows the method adopted in [53], where the authors demonstrate accurate force tracking of a robot arm in contact with surfaces of unknown linear compliance. Here, the same strategy is adapted to control the interaction torque between exoskeleton and human. Unlike [11], where a predefined and fixed torque reference is used, the present control provides adaptive assistance to the wearer based on the biomechanics model for both squatting and stooping.

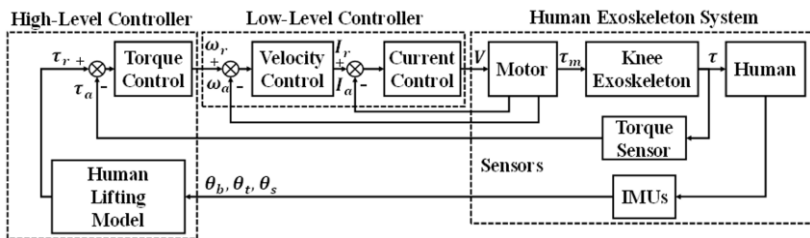


Fig. 10 Block diagram of the assistance control algorithm. The high-level controller generates a reference torque profile based on the biomechanics model. τ , I and ω denote the torque, the current and the velocity, respectively. V and τ_m are the motor input voltage and output torque. θ_b , θ_t , and θ_s denote the trunk, thigh and shank angles. Subscripts r and a refer to the reference and actual values, respectively.

The high-level controller runs at 1 kHz and implements a torque loop proportional-integral-derivative (PID) scheme to track the reference assistive torque.

The low-level controller instead implements a velocity loop PID scheme running at 20 kHz, and a current PID control running at 200 kHz. It measures real-time the motor status (i.e. current, velocity, and position) and communicates with the target computer through CAN bus.

Besides, three IMU sensors, five EMG sensors, and one loadcell are connected to the computer through corresponding interface boards. The IMUs provide measurements of the trunk angle θ_b , thigh angle θ_t , and shank angle θ_s with a sampling rate of 400 Hz.

470 They are calibrated to zero degrees at the beginning of the experiment, while the subject is instructed to stand straight. Then, the knee angle θ_k and hip angle θ_h are calculated by Eqs. (25)-(26) and their positive directions represent an extension.

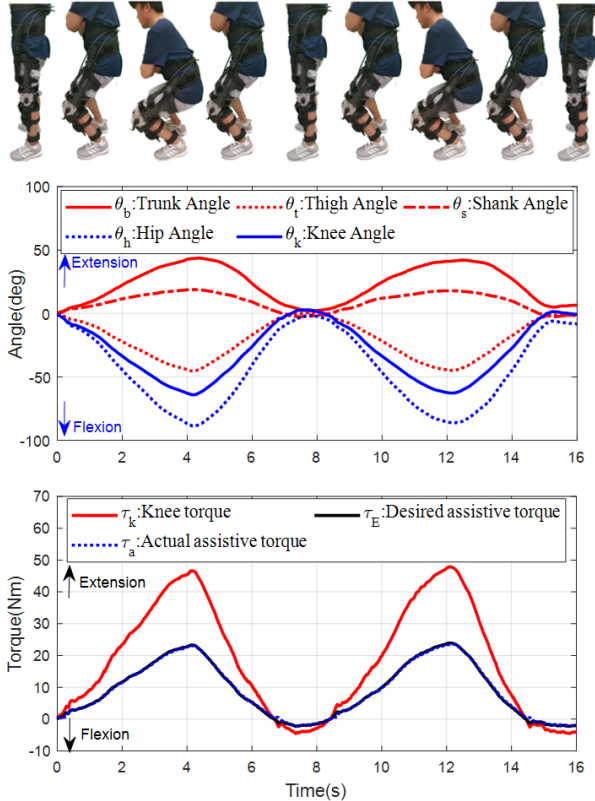
$$\theta_k = \theta_t - \theta_s \quad (25)$$

$$\theta_h = \theta_t - \theta_b \quad (26)$$

3.2.4 *Evaluation*

Several experiments were carried out to demonstrate the compliance of the exoskeleton, the control effectiveness, and the torque tracking performance.

475 The study was approved by the City University of New York Institutional Review Board, and all methods were carried out in accordance with the approved study protocol. Based on the experimental procedure, three healthy subjects performed 5 repetitions of squat motion. The rhythm was marked by a metronome and each cycle took 8 seconds, as shown in Fig. 11.



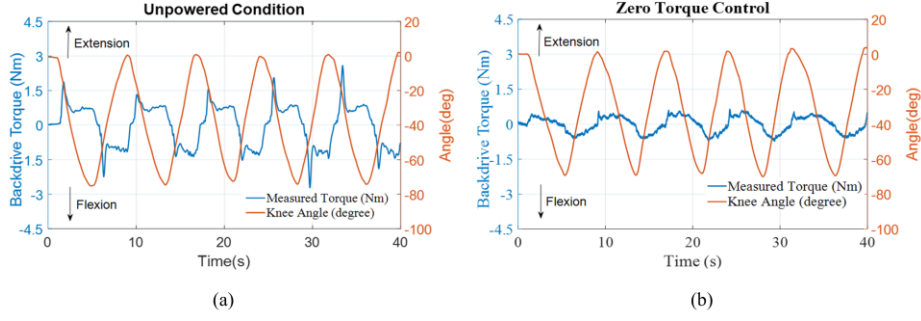
480

Fig. 11 Squat assistance control strategy. The top graph plots the evolution over time of the trunk, hip, thigh, knee and shank angles during two squatting cycles. The bottom graph reports the corresponding estimate of the required knee joint torque, and both the desired and actual assistive torques in the case of 50% level of assistance.

485

For the compliance evaluation, the back-drive torque was measured during squatting in unpowered condition. Thanks to the high torque density motor, the low gear ratio transmission and low-friction cable-drive mechanism, a very low mechanical impedance is obtained, as shown in Fig. 12(a). The peak back-drive torque is registered at the onset of motor rotation and in correspondence to the changes of direction. The average resistant torque is 0.92 Nm, while its maximum value is 2.58 Nm, much lower than other state-of-the-art knee exoskeletons (for instance, as an example case the corresponding peak resistance in [29] is 8 Nm). These results were confirmed also by the subjects, that reported extremely low resistance while wearing the device.

490



495

Fig. 12 Characterization of the mechanical impedance during squatting in the case of unpowered condition (a) and zero torque tracking control (b). The orange line is used for the knee angle, while the blue one for the measured resistant torque. The peak back-drive torque is registered at the onset of motor rotation and in correspondence to the changes of direction. The average back-drive torque is 0.92 Nm in case (a) and 0.34 in case (b), while the peak values are 2.58 Nm and 0.64 Nm, respectively.

500

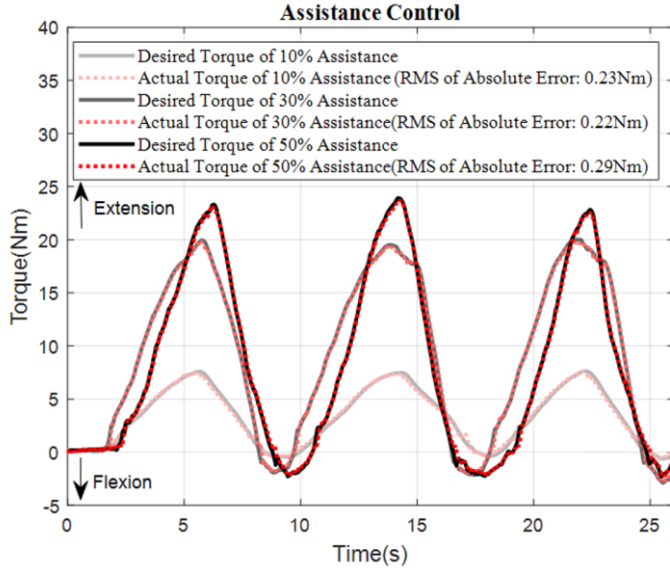
505

The same test was performed also with zero torque tracking control, whereby the resistant torque was measured while the actuator turned on and the reference torque was steadily set to zero, regardless of human motion. This trial was implemented to compensate for the mechanical resistance, such as friction of the cable and gears. Accordingly, the mechanical impedance was further reduced compared to the unpowered condition, as shown in Fig. 12(b). The average resistant torque is 0.34 Nm (4 times lower), while its maximum value is 0.64 Nm (2.7 times lower).

510

515

As a further evaluation, the torque tracking performance during squatting was analyzed for three levels of assistance, namely 10%, 30% and 50% of the required knee joint torque calculated by Eq. 18, corresponding to $\alpha = 0.1$, $\alpha = 0.3$ and $\alpha = 0.5$ in Eq. 24, respectively. Therefore, the assistive control was used to augment human knee joints during squats by applying specific torque depending on the current trunk angle θ_b and thigh angle θ_t detected by the IMU sensors. The tracking performance is shown in Fig. 13.



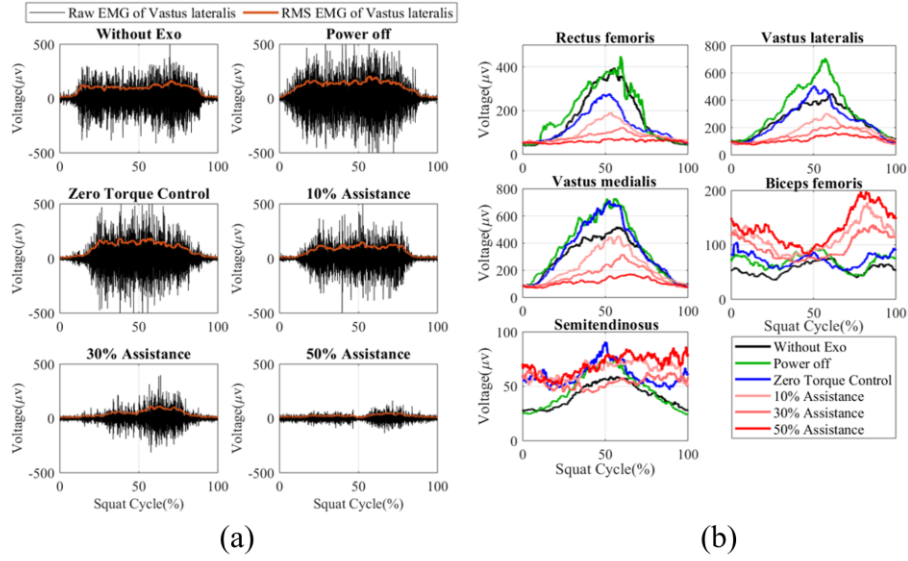
520 Fig. 13 Tracking performance of 10%, 30% and 50% knee torque assistance in three squatting cycles. The RMSE between the desired and actual torque trajectory is 0.23 Nm, 0.22 Nm, and 0.29 Nm, respectively. Overall RMSE of torque tracking is less than 0.29 Nm (1.21% of 24 Nm peak torque).

525 The RMSE between the desired and actual torque trajectory is 0.23 Nm (2.8% of 7.6 Nm peak torque), 0.22 Nm (1.1% of 20 Nm peak torque), and 0.29 Nm (1.2% of 23.9 Nm peak torque) in 10%, 30% and 50% knee assistance, respectively. These results demonstrate that the torque controller can deliver the desired torque profile with higher accuracy than other state-of-the-art devices: the overall RSME of torque tracking is about 0.29 Nm (1.2% of the peak torque) while for instance in [54] it is 2.1 Nm (21% error of 10 Nm peak torque).

Finally, the effectiveness of the assistance provided by the exoskeleton was evaluated in terms of its capability to reduce muscle activity.

530 For this purpose, the knee extensors (rectus femoris, vastus lateralis, vastus medialis) and the knee flexors (biceps femoris and semitendinosus) EMG signals were observed in six different scenarios: without the exoskeleton, power-off exoskeleton, zero torque control assistance, 10%, 30%, and 50% assistance.

Fig. 14(a) reports the data relative to the vastus lateralis of a single subject.



535

540

Fig. 14 Muscle activities during squatting in six different conditions: without-exoskeleton, power-off, zero torque control, 10%, 30%, and 50% assistance. (a) The vastus lateralis EMG of a single subject is plotted. It reveals that the assistive control has the beneficial effect of reducing the effort of the vastus lateralis muscle. (b) EMG data of knee extensor (rectus femoris, vastus lateralis, and vastus medialis) and flexor (biceps femoris and semitendinosus) muscles during squatting in different conditions. Lines represent the average RMS EMG from 15 squat cycles (5 squat cycles per three subjects). Results show that due to exoskeleton assistance activities of the knee extensor muscles were reduced, while those of flexor muscles were increased.

545

550

It shows that in the passive condition, due to the mechanical impedance of the wearable structure EMG amplitude of power-off condition is slightly higher than the one without the exoskeleton. In the active condition instead, the EMG amplitude of the zero torque control is pretty similar to the one without the exoskeleton, while it is clearly reduced in 10%, 30%, and 50% assistance. Therefore, these results reveal that the assistive control is effective in reducing the effort of the knee extensor muscle.

In an attempt to analyze the assistive effect in a more comprehensive way, Table III and Fig. 14(b) report the RMS amplitude of the EMG signals of the five observed muscles for each of the six conditions, whereby data are averaged over 15 squat cycles (5 squat cycles per 3 subjects). It turns out that EMG of knee extensors (rectus femoris, vastus lateralis, vastus medialis) reach the highest amplitude in power-off condition, but they are pretty similar to the cases without exoskeleton and with zero

torque control. Meanwhile, it is clear that the higher torque is delivered to the wearer, the lower is the muscle activity of the knee extensors. However, on the other side, an increase in the muscle activities of knee flexors (biceps femoris and semitendinosus) is observed. This is possibly due to the lack of training by the novice users of the exoskeleton, but there will need further investigation for a precise clarification.

TABLE III AVERAGE RMS EMG IN KNEE MUSCLES

Muscles	Sub.	WO	Off	0%	10%	30%	50%
Knee Extensors	Rectus Femoris	S1	78	87	35	25	28
	Rectus Femoris	S2	31	36	45	26	15
	Rectus Femoris	S3	56	65	49	46	35
	Rectus Femoris	Avg.	55	62	43	32	26
	Vastus Lateralis	S1	123	149	108	50	47
	Vastus Lateralis	S2	44	51	61	39	20
	Vastus Lateralis	S3	89	124	81	79	72
	Vastus Lateralis	Avg.	85	108	83	56	46
	Vastus Medialis	S1	87	124	111	50	46
	Vastus Medialis	S2	98	117	135	78	38
	Vastus Medialis	S3	112	129	101	98	88
	Vastus Medialis	Avg.	99	124	116	75	54
	Knee Extensors	80	98	80	55	42	30
Knee Flexors	Biceps Femoris	S1	23	25	23	63	43
	Biceps Femoris	S2	13	20	18	13	16
	Biceps Femoris	S3	20	25	32	37	55
	Biceps Femoris	Avg.	19	23	24	38	32
	Semitendinosus	S1	13	14	11	20	15
	Semitendinosus	S2	14	19	19	14	14
	Semitendinosus	S3	15	14	30	31	24
	Semitendinosus	Avg.	14	16	20	22	18
	Knee Flexors	16	19	22	30	25	34

Unit (μ V); WO (Without Exo); Off (Power off); 0% (Zero Torque);
10% (10% Assistance); 30% (30% Assistance); 50% (50% Assistance)

In summary, experimental results indicate that the proposed exoskeleton is highly-backdrivable with minute mechanical resistance and that moderate levels of assistance can effectively reduce muscles efforts during squatting. In particular, it was observed that the proposed exoskeleton can reduce the knee extensors activity, but it is still not clear if the work is globally alleviated or simply transferred to adjacent muscle groups (e.g. hip extensors, hip flexors, ankle extensors, and ankle flexors), due to the complex mechanism of muscle group compensation. Metabolics measurements will be used in the future to perform a more in-depth analysis of the actual efficacy.

3.3 Back Exoskeleton

Back injuries are the most prevalent work-related musculoskeletal disorders [55].
575 Wearable robots present an attractive solution to mitigate ergonomic risk factors and reduce musculoskeletal loading for workers who perform lifting. Over the last two decades, various studies have demonstrated that industrial exoskeletons can decrease total work, fatigue, and load while increasing productivity and work quality [1, 56]. For instance, Toxiri et al. developed a powered back-support exoskeleton that reduced
580 30% muscular activity at the lumbar spine [4], while a passive back exoskeleton with a larger range of motion of the trunk was proposed in [57]. The key challenges of back-support exoskeleton lie in the unique anatomy of the human spine, composed of 23 intervertebral discs. Therefore, this structure imposes stringent requirements that necessitate new solutions for effective human-robot interaction.

585 To address the aforementioned challenge, a spine-inspired continuum soft exoskeleton has been developed with the aim of reducing spine loading during stoop lifting while not limiting the natural movements. In particular, the stoop lifting induces extension and flexion of the lumbar joints with 70° in the sagittal plane. Moreover, the natural range of motion allows lateral flexion of 20° in the frontal plane
590 and rotation of 90° in the transverse plane. Biomechanics analysis reveals that 250 N of the exoskeleton force perpendicular to the back can decrease 30% of the lumbar compression force at the lumbosacral joint (L5/S1, between 5th lumbar and 1st sacral) while a 15 kg load is lifted.

3.3.1 *Design*

595 Due to the requirement of having a system conformal to the human back anatomy and unobtrusive for the natural movements, the proposed robot leverages on a hyper-redundant continuum structure that is able to continuously bend [58], as shown in Fig. 15(a).



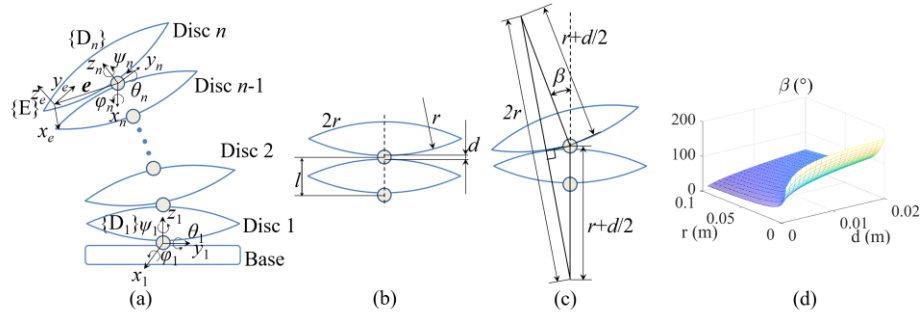
600 Fig. 15 (a) The spine-inspired back exoskeleton leverages on a hyper-redundant continuum
 mechanism. Thanks to its compliance, this wearable robot provides assistive force while being
 conformal to the anatomy of the human back and unobtrusive for natural motion. (b) A healthy
 605 subject wearing the back exoskeleton to perform stoop lifting of a 15 kg load. The spine
 continuum mechanism is powered by a tethered actuation platform via Bowden cable
 transmission.

610 Additionally, Fig. 15(b) shows the overall setup, which includes a wearable
 structure made of shoulder and waist braces, the high torque density actuator
 implemented as a tethered platform, the Bowden cable transmission, and the control
 system. The spinal structure is a cable-driven mechanism and has a modular
 615 architecture composed of twenty segments. Each segment is comprised of a disc that
 pivots on a ball and socket joint. Thus, each pair of neighboring disks form a three-
 DOF spherical joint. A cable is threaded through holes at the edges of the discs, so
 that when the actuator pulls the cable, the discs rotate about the ball joint, acting as
 620 levers and producing assistive torque on the human. The electric motor delivers 2 Nm
 nominal torque at 1500 rpm nominal speed, and it is coupled to a gearbox with a 36:1
 gear ratio. As a result, the actuation platform can output up to 1500 N pulling force at
 0.22 m/s cable translating speed. A customized load cell placed at the bottom of the
 spinal structure allows to measure the cable tension. Moreover, an elastic backbone
 integration of the overall mechanism.

3.3.2 Modeling

A kinematics analysis is carried out to optimize the geometrical design and to characterize the range of motion of the mechanism.

625 The configuration of the back exoskeleton is determined by the accumulated rotations of all discs, as shown in Fig. 16(a).



630 Fig. 16 Kinematics analysis of the spine continuum structure. (a) The configuration of the exoskeleton is determined by the accumulated rotations of all the discs. (b) Initial configuration of two adjacent discs. (c) Extreme configuration of two adjacent discs due to a mechanical contact constraint. (d) Variation of β (maximal rotation angle between two neighboring discs) with respect to the geometric parameters r (radius of the disc) and d (distance between two neighboring discs). β affects the range of motion of the exoskeleton.

635 The pose of the $(i+1)^{\text{th}}$ disc with respect to the i^{th} disc can be represented by the homogeneous transformation

$$T_{i+1} = \text{Rot}_x(\varphi_{i+1}) \text{Rot}_y(\theta_{i+1}) \text{Rot}_z(\psi_{i+1}) \text{Tran}(\mathbf{l}), \quad (27)$$

640 where φ_{i+1} , θ_{i+1} , ψ_{i+1} are the rotation angles of disc $i+1$ with respect to disc i in the sagittal, frontal and transverse planes, respectively, and $\mathbf{l} = (0 \ 0 \ l)^T$ is the distance vector between two neighboring discs. $\text{Rot}_x(\cdot)$, $\text{Rot}_y(\cdot)$, $\text{Rot}_z(\cdot)$ denote 4×4 homogeneous transformation matrices representing rotations around x, y and z axes, respectively, while $\text{Tran}(\cdot)$ is a 4×4 homogeneous translation matrix.

By putting all together, the global pose transformation of the mechanism from the base to the distal disc n can be calculated by

$$T_{tot} = T_1 T_2 \cdots T_n. \quad (28)$$

From (28) we see that the overall range of motion is the accumulation of the ranges of motion of individual discs. The range of motion of one disc with respect to the adjacent disc depends on the geometric parameters of the disc and the spherical joint in between. When the disc rotates from the initial configuration represented in Fig. 16(b) to the extreme configuration due to a mechanical contact constraint, as depicted in Fig. 16(c), the maximal rotation angle β can be calculated by

$$\beta = \pi - 2 \arcsin \left(\frac{r}{(r + \frac{d}{2})} \right). \quad (29)$$

In (29), r denotes the radius of the disc, d is the distance between two neighboring discs and l is the distance between the centers of two neighboring spherical joints.

Accordingly, the range of motion, related to β , can be designed by adjusting the parameters r and d . Fig. 16(d) shows the effect of these two parameters on β .

For the present design it was chosen $r = 0.07$ m and $d = 0.00216$ m to obtain $\beta = 20^\circ$, that allows to satisfy all the motion requirements (i.e. forward flexion of 70° in the sagittal plane, lateral flexion of 20° in the frontal plane and rotation of 90° in the transverse plane) with a number of discs greater than 6.

Given the kinematics characterization of the robot mechanism, it is crucial to examine a biomechanics model of human-robot interaction to facilitate the development of assistive control of the soft exoskeleton.

The kinetic purpose of the back exoskeleton is to reduce the compression and shear forces between discs, which are the main causes of low back pain. Therefore, a basic analytical model of the forces acting on the human spine is derived to predict the effectiveness of the exoskeleton assistance on reducing the forces in the human spine and muscles.

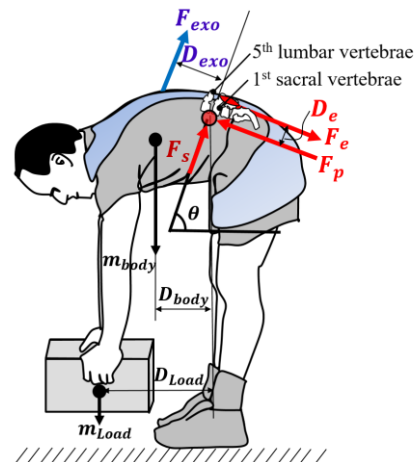
For the sake of simplicity, the lumbar spine is modeled as a localized joint at the lumbar-sacral interface (L5/S1). Then, consider the condition when the human is in the flexed forward position during stoop lifting, as illustrated in Fig. 17. The static equilibrium analysis provides the relationship between exoskeleton assistance and the forces in the human spine:

$$F_e D_e = -F_{exo} D_{exo} + m_{load} g D_{load} + m_{body} g D_{body} \quad (30)$$

$$F_p = F_e + m_{body} g \cos \theta + m_{load} g \cos \theta \quad (31)$$

$$F_s = -F_{exo} + m_{body} g \sin \theta + m_{load} g \sin \theta \quad (32)$$

675 F_p , F_s denote the compressive and shear forces of intervertebral discs, F_{exo} is the force applied by the back exoskeleton, and F_e denotes the force of the erector spinae muscle. m_{body} and m_{load} are the masses of the human upper body and of the load, respectively. D_{exo} , D_e , D_{load} , D_{body} are the moment arms of the exoskeleton, erector spinae muscle, load, and upper body, respectively.



680 Fig. 17 Biomechanics model of human-robot interaction during stoop lifting. If the exoskeleton applies a force perpendicular to the human back, it has the effect of accordingly reducing the spine compression force, the intervertebral shear force, and the lumbar muscle force.

According to (30)-(32), it can be observed that if the exoskeleton force F_{exo} increases, the erector muscle force F_e , the spine compressive force F_p , and the intervertebral shear force F_s decrease simultaneously, because the weights of the human and of the load are partly balanced by the assistive force of the exoskeleton.

The control architecture, as shown in Fig. 18(a), consists of two main layers: a high-level controller and a low-level controller.

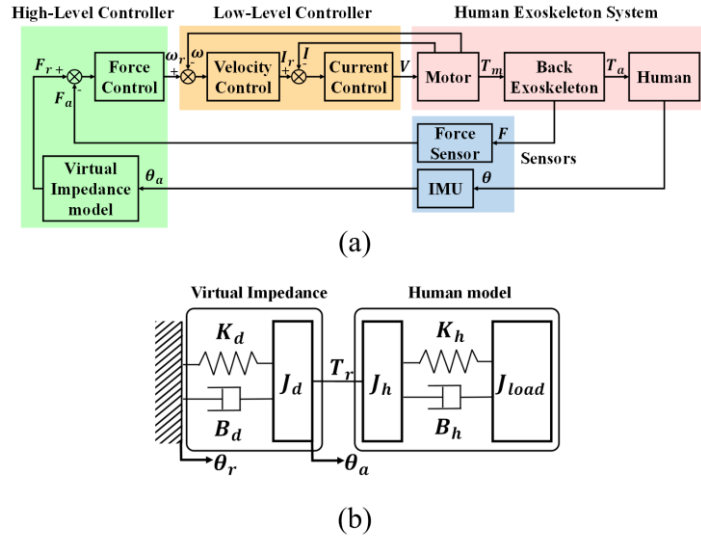


Fig. 18 (a) Block diagram of the back exoskeleton control architecture for stoop assistance. It consists of two main controllers: the high-level controller receives sensor measurements about the cable force and the human trunk motion and generates the reference assistive force through the virtual impedance model, while the low-level controller implements motor velocity and current control. (b) Virtual impedance model. The assistive torque is generated by Eq. (33) from the desired reference position trajectory and the actual position trajectory with the desired stiffness K_d , damping B_d , and inertia J_d . Using the virtual impedance model, the exoskeleton generated an assistive torque reference T_r .

In the high-level controller a virtual impedance model, represented in Fig. 18(b), is used to generate the reference assistive force according to Eq. (33).

$$F_r = \frac{T_r}{r_1} = \frac{1}{r_1} [J_d(\ddot{\theta}_a - \ddot{\theta}_r) + B_d(\dot{\theta}_a - \dot{\theta}_r) + K_d(\theta_a - \theta_r)], \quad (33)$$

where θ_r , $\dot{\theta}_r$, and $\ddot{\theta}_r$ denote the desired trunk angle, velocity, and acceleration, generated from a predefined desired trajectory, while θ_a , $\dot{\theta}_a$, and $\ddot{\theta}_a$ are the actual values measured by an IMU sensor mounted on the trunk. In this case, the desired trajectory is set to zero, so that virtual spring and damper are fixed to the ground.

705 High-level control is implemented in Matlab/Simulink Real-Time and operates at 1000 Hz frequency. A PID force control is used to ensure that the cable measured force tracks the reference force F_r .

710 In the low-level controller, a DSP microcontroller (TMS320F28335, Texas Instruments, USA) is used for motor current and velocity control. It uses CAN bus communication to receive the desired velocity command V_r and to send data about the actuator state. Both velocity and current controllers implement a PID algorithm to track the reference signals.

715 Regarding the sensing system, a data acquisition (I/O) card (ADC, PCIe-6259, National Instrument, Inc., USA) is used to acquire cable force measurements from the loadcell mounted on the back exoskeleton, while an IMU mounted on the subject trunk transmits the trunk motion data (angle, angular velocity, and angular acceleration) via serial port (RS-232) to the target computer.

3.3.4 *Evaluation*

720 The exoskeleton provides assistance in stoop lifting without limiting natural motion. As shown in Fig. 19, the wearer is free to perform forward flexion, lateral flexion, and rotation.

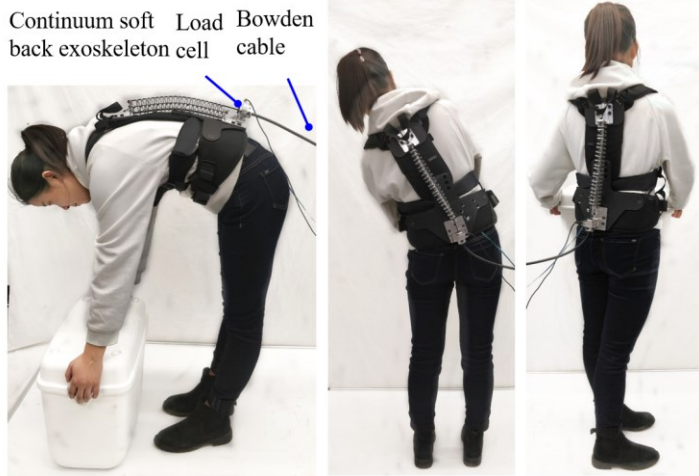


Fig. 19 The continuum soft exoskeleton assists human stoop lifting while imposing no constraints on human forward flexion (left), lateral flexion (middle) and rotation (right).

725 Fig. 15(b) shows the setup used for the experimental evaluation of the back exoskeleton. Besides the wearable structure, it includes the Bowden cable transmission, the tethered actuation platform, and the real-time control system. Currently, a tethered actuation system is employed to perform a proof of concept trial, aimed at demonstrating the feasibility of the proposed spine design and control algorithm, thus minimizing the impact of the mass of the system. However, it is worth 730 highlighting that the combined mass of motor and gearbox is just 0.55 kg, hence a portable version is indeed a practicable advancement already under development.

735 Three subjects performed 10 repetitions of 15 kg stoop lifting. Each stoop cycle took 8 seconds: 4 seconds for bending forward from stand-up posture to trunk flexion and 4 seconds for extending back from trunk flexion to stand-up posture. The study methods were carried out in accordance with the approved study protocol.

The first test regarded the steerability evaluation of the continuum exoskeleton, that is the relation between the cable displacement and the bending angle of the back exoskeleton, defined as the angle between the end faces of the base and the top disc.

740 Results shown in Fig. 20 indicate that a cable displacement of 5.23 cm produces a bending angle of 100°, which is beyond the required range of motion of 70°.

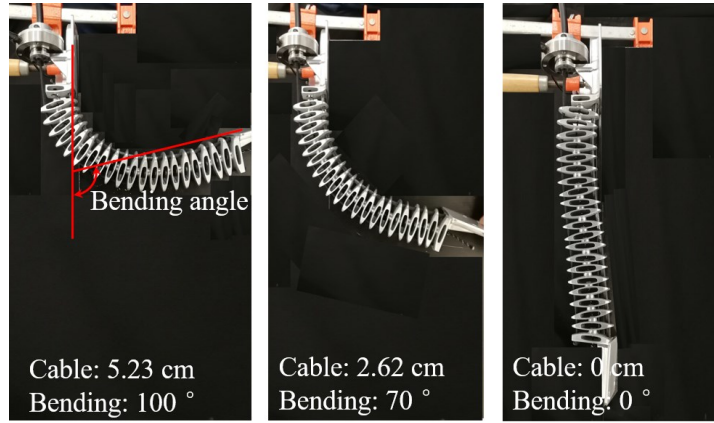


Fig. 20 The steerability sequence of the continuum exoskeleton. The bending angle is defined as the angle between the end faces of the base and the top disc. A cable displacement of 5.23 cm is sufficient to produce a bending angle of 100°.

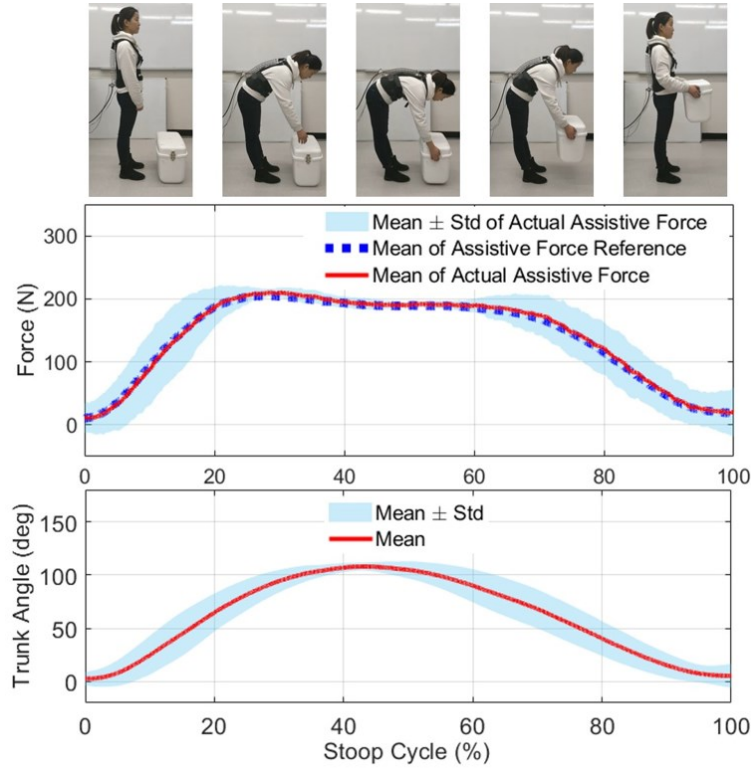
745

Then, the tracking performance of the assistive force control is evaluated. The desired assistance is calculated according to the virtual impedance model described by

$$F_r = 20\dot{\theta}_a + 200 \sin \theta_a, \quad (34)$$

750

where the sine function in the stiffness term has the function of compensating the involved components (which are related to $\sin \theta_a$) of the human and load gravity terms. Fig. 21 illustrates the variation of the force and the trunk angle during the stoop task, as observed from a total of 30 stoop cycles executed by three different subjects.



755 Fig. 21 Assistive force tracking performance and trunk angle measurement during stoop lifting. Tests were executed by three healthy subjects and each subject performed 10 stoop cycles, for a total of 30 stoop repetitions. The mean actual assistive force (red solid line) is able to accurately track the mean reference assistive force (blue dashed line). The light blue area identifies the variation within ± 1 standard deviation. RMSE of force tracking is 6.63 N (3.3% of the 200 N peak force).

760 The RMSE of force tracking is 6.63 N (3.3% of the 200 N peak force). Therefore, regardless of motion variability (represented by the standard deviation of trunk angles), the implemented controller was able to successfully track the desired force with high accuracy.

4. Discussion

765 This chapter presented the advanced QDD actuation paradigm for high-performance wearable robots. Based on an ad-hoc customized motor and low ratio

gear transmission it ensures large versatility thanks to high torque density (20.7 Nm/kg), high backdrivability (0.4 Nm back-drive torque in unpowered mode) and high bandwidth (62.4 Hz). These properties are well suitable for applications involving human-robot interaction. Therefore, taking advantage of these 770 characteristics three exoskeletons have been designed to provide assistance to the hip, the knee and the back. Their feasibility and effectiveness were experimentally tested on healthy subjects. All of them exhibited low mechanical impedance and high accuracy in assistive force tracking, being able to overcome the performance of analogous state-of-the-art devices. In particular, the bilateral hip exoskeleton achieved 775 0.4 Nm back-drive torque, 62.4 Hz bandwidth, and RMSE in force tracking equal to 5.4% of 20 Nm peak torque. The bilateral knee exoskeleton instead presented back-drive torque equal to 1.5 Nm in unpowered mode and 0.5 Nm with zero-torque tracking control, while RMSE of torque tracking was 1.2% of 24 Nm peak torque. Finally, for the spine exosuit RMSE of force tracking was about 3.3% of the 200N 780 peak force. In conclusion, experimental results prove that the presented actuation paradigm offers promising features to push the limits of wearable robots' performance. QDD actuation constitutes an enabling technology that could pave the way to the development of more lightweight, more compliant, safer and stronger exoskeletons for either rehabilitation or augmentation purposes.

785 **Acknowledgments**

This work is supported by the National Science Foundation (NSF) grant IIS 1830613, CMMI 1944655, NIH R01EB029765, and Grove School of 790 Engineering, The City University of New York, City College. Any opinions, findings, and conclusions or recommendations expressed in this material are those of the author(s) and do not necessarily reflect the views of the funding organizations.

References

795 [1] Michiel P De Looze, Tim Bosch, Frank Krause, Konrad S Stadler, and Leonard W O'Sullivan. Exoskeletons for industrial application and their potential effects on physical work load. *Ergonomics*, 59(5):671–681, 2016.

800 [2] Ye Ding, Myunghee Kim, Scott Kuindersma, and Conor J Walsh. Human-in-the-loop optimization of hip assistance with a soft exosuit during walking. *Science Robotics*, 3(15):eaar5438, 2018.

805 [3] Zachary F Lerner, Diane L Damiano, and Thomas C Bulea. A lower-extremity exoskeleton improves knee extension in children with crouch gait from cerebral palsy. *Science translational medicine*, 9(404):eaam9145, 2017.

[4] Stefano Toxiri, Axel S Koopman, Maria Lazzaroni, Jesús Ortiz, Valerie Power, Michiel P de Looze, Leonard O'Sullivan, and Darwin G Caldwell. Rationale, implementation and evaluation of assistive strategies for an active back-support exoskeleton. *Frontiers in Robotics and AI*, 5:53, 2018.

810 [5] Jonathan C Mcleod, Susie JM Ward, and Audrey L Hicks. Evaluation of the keeogo™ dermoskeleton. *Disability and Rehabilitation: Assistive Technology*, 14(5):503–512, 2019.

[6] Saivimal Sridar, Pham H Nguyen, Mengjia Zhu, Quoc P Lam, and Panagiotis Polygerinos. Development of a soft-inflatable exosuit for knee rehabilitation. In *2017 IEEE/RSJ International Conference on Intelligent Robots and Systems (IROS)*, pages 3722–3727. IEEE, 2017.

815 [7] James S Sulzer, Ronald A Roiz, Michael A Peshkin, and James L Patton. A highly backdrivable, lightweight knee actuator for investigating gait in stroke. *IEEE Transactions on Robotics*, 25(3):539–548, 2009.

[8] BT Quinlivan, S Lee, P Malcolm, DM Rossi, M Grimmer, C Siviy, N Karavas, D Wagner, A Asbeck, I Galiana, et al. Assistance magnitude versus metabolic cost reductions for a tethered multiarticular soft exosuit. *Sci. Robot*, 2(2):1–10, 2017.

820 [9] Jinsoo Kim, Giuk Lee, Roman Heimgartner, Dheepak Arumukhom Revi, Nikos Karavas, Danielle Nathanson, Ignacio Galiana, Asa Eckert-Erdheim, Patrick Murphy, David Perry, et al. Reducing the metabolic rate of walking

and running with a versatile, portable exosuit. *Science*, 365(6454):668–672, 2019.

825 [10] Elena Martini, Simona Crea, Andrea Parri, Luca Bastiani, Ugo Faraguna, Zach McKinney, Raffaello Molino-Lova, Lorenza Pratali, and Nicola Vitiello. Gait training using a robotic hip exoskeleton improves metabolic gait efficiency in the elderly. *Scientific reports*, 9(1):1–12, 2019.

830 [11] Baojun Chen, Lorenzo Grazi, Francesco Lanotte, Nicola Vitiello, and Simona Crea. A real-time lift detection strategy for a hip exoskeleton. *Frontiers in neurorobotics*, 12:17, 2018.

835 [12] Florian L Haufe, Alessia M Kober, Kai Schmidt, Alejandro Sancho-Puchades, Jaime E Duarte, Peter Wolf, and Robert Riener. User-driven walking assistance: first experimental results using the myosuit. In *2019 IEEE 16th International Conference on Rehabilitation Robotics (ICORR)*, pages 944–949. IEEE, 2019.

[13] Andrés Martnez, Brian Lawson, and Michael Goldfarb. A controller for guiding leg movement during overground walking with a lower limb exoskeleton. *IEEE Transactions on Robotics*, 34(1):183–193, 2017.

840 [14] Patrick M Wensing, Albert Wang, Sangok Seok, David Otten, Jeffrey Lang, and Sangbae Kim. Proprioceptive actuator design in the mit cheetah: Impact mitigation and high-bandwidth physical interaction for dynamic legged robots. *IEEE Transactions on Robotics*, 33(3):509–522, 2017.

845 [15] Shuangyue Yu, Tzu-Hao Huang, Dianpeng Wang, Brian Lynn, Dina Sayd, Viktor Silivanov, Young Soo Park, Yingli Tian, and Hao Su. Design and control of a high-torque and highly backdrivable hybrid soft exoskeleton for knee injury prevention during squatting. *IEEE Robotics and Automation Letters*, 4(4):4579–4586, 2019.

850 [16] Sangok Seok, Albert Wang, Meng Yee Michael Chuah, Dong Jin Hyun, Jongwoo Lee, David M Otten, Jeffrey H Lang, and Sangbae Kim. Design principles for energy-efficient legged locomotion and implementation on the mit cheetah robot. *Ieee/asme transactions on mechatronics*, 20(3):1117–1129, 2014.

855 [17] Jose L Contreras-Vidal, Nikunj A Bhagat, Justin Brantley, Jesus G Cruz-Garza, Yongtian He, Quinn Manley, Sho Nakagome, Kevin Nathan, Su H Tan, Fangshi Zhu, et al. Powered exoskeletons for bipedal locomotion after spinal cord injury. *Journal of neural engineering*, 13(3):031001, 2016.

860 [18] Xiang Li, Yongping Pan, Gong Chen, and Haoyong Yu. Multi-modal control scheme for rehabilitation robotic exoskeletons. *The International Journal of Robotics Research*, 36(5-7):759–777, 2017.

[19] Inseung Kang, Hsiang Hsu, and Aaron Young. The effect of hip assistance levels on human energetic cost using robotic hip exoskeletons. *IEEE Robotics and Automation Letters*, 4(2):430–437, 2019.

865 [20] Jaehyun Bae, Christopher Siviy, Michael Rouleau, Nicolas Menard, Kathleen O’Donnell, Ignacio Geliana, Maria Athanassiu, Danielle Ryan, Christine Bibeau, Lizeth Sloot, et al. A lightweight and efficient portable soft exosuit for paretic ankle assistance in walking after stroke. In *2018 IEEE International Conference on Robotics and Automation (ICRA)*, pages 2820–2827. IEEE, 2018.

870 [21] Younbaek Lee, Se-gon Roh, Minhyung Lee, Byungjune Choi, Jongwon Lee, Jeonghun Kim, Hyundo Choi, Youngbo Shim, and Yong-Jae Kim. A flexible exoskeleton for hip assistance. In *2017 IEEE/RSJ International Conference on Intelligent Robots and Systems (IROS)*, pages 1058–1063. IEEE, 2017.

875 [22] Tommaso Lenzi, Maria Chiara Carrozza, and Sunil K Agrawal. Powered hip exoskeletons can reduce the user’s hip and ankle muscle activations during walking. *IEEE Transactions on Neural Systems and Rehabilitation Engineering*, 21(6):938–948, 2013.

880 [23] Ting Zhang and He Huang. A lower-back robotic exoskeleton: Industrial handling augmentation used to provide spinal support. *IEEE Robotics & Automation Magazine*, 25(2):95–106, 2018.

[24] Nicholas Paine, Sehoon Oh, and Luis Sentis. Design and control considerations for high-performance series elastic actuators. *IEEE/ASME Transactions on Mechatronics*, 19(3):1080–1091, 2013.

885 [25] Joshua M Caputo and Steven H Collins. Prosthetic ankle push-off work reduces metabolic rate but not collision work in non-ampetee walking. *Scientific reports*, 4(1):1–9, 2014.

890 [26] Giuk Lee, Ye Ding, Ignacio Galiana Bujanda, Nikos Karavas, Yu Meng Zhou, and Conor J Walsh. Improved assistive profile tracking of soft exosuits for walking and jogging with off-board actuation. In *2017 IEEE/RSJ International Conference on Intelligent Robots and Systems (IROS)*, pages 1699–1706. IEEE, 2017.

895 [27] Xiaolong Yang, Tzu-Hao Huang, Hang Hu, Shuangyue Yu, Sainan Zhang, Xianlian Zhou, Alessandra Carriero, Guang Yue, and Hao Su. Spine-inspired continuum soft exoskeleton for stoop lifting assistance. *IEEE Robotics and Automation Letters*, 4(4):4547–4554, 2019.

900 [28] Yanran Ding and Hae-Won Park. Design and experimental implementation of a quasi-direct-drive leg for optimized jumping. In *2017 IEEE/RSJ International Conference on Intelligent Robots and Systems (IROS)*, pages 300–305. IEEE, 2017.

905 [29] Ge Lv and Robert D Gregg. Underactuated potential energy shaping with contact constraints: Application to a powered knee-ankle orthosis. *IEEE Transactions on Control Systems Technology*, 26(1):181–193, 2017.

[30] Junlin Wang, Xiao Li, Tzu-Hao Huang, Shuangyue Yu, Yanjun Li, Tianyao Chen, Alessandra Carriero, Mooyeon Oh-Park, and Hao Su. Comfort-centered design of a lightweight and backdrivable knee exoskeleton. *IEEE Robotics and Automation Letters*, 3(4):4265–4272, 2018.

910 [31] Thomas Reichert, Thomas Nussbaumer, and Johann W Kolar. Torque scaling laws for interior and exterior rotor permanent magnet machines. *A A*, 3:1, 2009.

[32] Jae Jun Lee, Won Ho Kim, Jin Seung Yu, Si Yeong Yun, Sang Min Kim, Jin Ju Lee, and Ju Lee. Comparison between concentrated and distributed winding in ipmsm for traction application. In *2010 International Conference on Electrical Machines and Systems*, pages 1172–1174. IEEE, 2010.

915 [33] Hanqi Zhu, Christopher Nesler, Nikhil Divekar, M Taha Ahmad, and Robert D Gregg. Design and validation of a partial-assist knee orthosis with

compact, backdrivable actuation. In *2019 IEEE 16th International Conference on Rehabilitation Robotics (ICORR)*, pages 917–924. IEEE, 2019.

920 [34] Jamie Wolff, Claire Parker, Jaimie Borisoff, W Ben Mortenson, and Johanne Mattie. A survey of stakeholder perspectives on exoskeleton technology. *Journal of neuroengineering and rehabilitation*, 11(1):169, 2014.

[35] Daniel J Gonzalez and H Harry Asada. Hybrid open-loop closed-loop control of coupled human–robot balance during assisted stance transition with extra robotic legs. *IEEE Robotics and Automation Letters*, 4(2):1676–1683, 2019.

925 [36] Wesley E Woodson, Barry Tillman, and Peggy Tillman. *Human factors design handbook: information and guidelines for the design of systems, facilities, equipment, and products for human use*. 1992.

[37] Keehong Seo, Jusuk Lee, and Young Jin Park. Autonomous hip exoskeleton saves metabolic cost of walking uphill. In *2017 International Conference on Rehabilitation Robotics (ICORR)*, pages 246–251. IEEE, 2017.

930 [38] Jusuk Lee, Keehong Seo, Bokman Lim, Junwon Jang, Kyungrock Kim, and Hyundo Choi. Effects of assistance timing on metabolic cost, assistance power, and gait parameters for a hip-type exoskeleton. In *2017 International Conference on Rehabilitation Robotics (ICORR)*, pages 498–504. IEEE, 2017.

935 [39] Jörn Malzahn, Navvab Kashiri, Wesley Roozing, Nikos Tsagarakis, and Darwin Caldwell. What is the torque bandwidth of this actuator? In *2017 IEEE/RSJ International Conference on Intelligent Robots and Systems (IROS)*, pages 4762–4768. IEEE, 2017.

940 [40] Jianfu Yang, Tzu-Hao Huang, Shuangyue Yu, Xiaolong Yang, Hao Su, Ann M Spungen, and Chung-Ying Tsai. Machine learning based adaptive gait phase estimation using inertial measurement sensors. In *2019 Design of Medical Devices Conference*. American Society of Mechanical Engineers Digital Collection, 2019.

945 [41] Xavier Glorot and Yoshua Bengio. Understanding the difficulty of training deep feedforward neural networks. In *Proceedings of the thirteenth*

international conference on artificial intelligence and statistics, pages 249–256, 2010.

950 [42] Andrew Stuart McIntosh, Karen T Beatty, Leanne N Dwan, and Deborah R Vickers. Gait dynamics on an inclined walkway. *Journal of biomechanics*, 39(13):2491–2502, 2006.

955 [43] Christopher R Reid, Pamela McCauley Bush, Nancy H Cummings, Dianne L McMullin, and Samiullah K Durrani. A review of occupational knee disorders. *Journal of occupational rehabilitation*, 20(4):489–501, 2010.

[44] Volker Bartenbach, Marcel Gort, and Robert Riener. Concept and design of a modular lower limb exoskeleton. In *2016 6th IEEE International Conference on Biomedical Robotics and Biomechatronics (BioRob)*, pages 649–654. IEEE, 2016.

960 [45] Tomislav Bacek, Marta Moltedo, Carlos Rodriguez-Guerrero, Joost Geeroms, Bram Vanderborght, and Dirk Lefeber. Design and evaluation of a torque-controllable knee joint actuator with adjustable series compliance and parallel elasticity. *Mechanism and Machine Theory*, 130:71–85, 2018.

965 [46] Nikos Karavas, Arash Ajoudani, Nikos Tsagarakis, Jody Saglia, Antonio Bicchi, and Darwin Caldwell. Tele-impedance based stiffness and motion augmentation for a knee exoskeleton device. In *2013 IEEE International Conference on Robotics and Automation*, pages 2194–2200. IEEE, 2013.

970 [47] Jerry E Pratt, Benjamin T Krupp, Christopher J Morse, and Steven H Collins. The roboknee: an exoskeleton for enhancing strength and endurance during walking. In *IEEE International Conference on Robotics and Automation, 2004. Proceedings. ICRA '04. 2004*, volume 3, pages 2430–2435. IEEE, 2004.

[48] Kirby Ann Witte, Andreas M Fatschel, and Steven H Collins. Design of a lightweight, tethered, torque-controlled knee exoskeleton. In *2017 international conference on rehabilitation robotics (ICORR)*, pages 1646–1653. IEEE, 2017.

975 [49] Tat Luat Nguyen, Samuel J Allen, and Soo Jay Phee. Direct torque control for cable conduit mechanisms for the robotic foot for footwear testing. *Mechatronics*, 51:137–149, 2018.

980 [50] Kyoungchul Kong, Joonbum Bae, and Masayoshi Tomizuka. Torque mode control of a cable-driven actuating system by sensor fusion. *Journal of Dynamic Systems, Measurement, and Control*, 135(3), 2013.

985 [51] Andrej Gams, Tadej Petric, Tadej Debevec, and Jan Babic. Effects of robotic knee exoskeleton on human energy expenditure. *IEEE Transactions on Biomedical Engineering*, 60(6):1636–1644, 2013.

990 [52] Harry G Armstrong. Anthropometry and mass distribution for human analogues. *Military male aviators*, 1, 1988.

[53] Jaydeep Roy and Louis L Whitcomb. Adaptive force control of position/velocity controlled robots: theory and experiment. *IEEE Transactions on Robotics and Automation*, 18(2):121–137, 2002.

995 [54] Inseung Kang, Hsiang Hsu, and Aaron J Young. Design and validation of a torque controllable hip exoskeleton for walking assistance. In *ASME 2018 Dynamic Systems and Control Conference*. American Society of Mechanical Engineers Digital Collection, 2018.

[55] Liberty Mutual Insurance. The most serious workplace injuries cost us companies 59.9 billion per year, according to 2017 liberty mutual workplace safety index, 2017.

1000 [56] Bruno R da Costa and Edgar Ramos Vieira. Risk factors for work-related musculoskeletal disorders: a systematic review of recent longitudinal studies. *American journal of industrial medicine*, 53(3):285–323, 2010.

[57] Matthias B Näf, Axel S Koopman, Saskia Baltrusch, Carlos Rodriguez-Guerrero, Bram Vanderborght, and Dirk Lefeber. Passive back support exoskeleton improves range of motion using flexible beams. *Frontiers in Robotics and AI*, 5:72, 2018.

1005 [58] Robert J Webster III and Bryan A Jones. Design and kinematic modeling of constant curvature continuum robots: A review. *The International Journal of Robotics Research*, 29(13):1661–1683, 2010.